Interlayer coupling in spin valves studied by broadband ferromagnetic resonance

D. E. Gonzalez-Chavez, R. Dutra, W. O. Rosa, T. L. Marcondes, A. Mello, and R. L. Sommer
Centro Brasileiro de Pesquisas Físicas, 22290-180 Rio de Janeiro, RJ, Brazil
(Received 10 June 2013; published 30 September 2013)

The magnetization dynamics of coupled and uncoupled spin valves with the structure NiFe (20 nm)/Cu(t_{Cu})/NiFe (20 nm)/IrMn (10 nm) is probed by broadband ferromagnetic resonance absorption measurements. The coupling intensity between the free and the pinned layers is tailored by varying the Cu thickness t_{Cu}. Broadband spectra exhibited two resonant modes for each value of the applied field. It is observed that the coupling between NiFe layers modifies the amplitude of the absorption peaks and the shape of the dispersion relations for each mode, which becomes particularly distorted in the antiparallel magnetization state. The observed phenomena are well described by applying a semianalytical model that properly takes into account the coupling interactions and allows an efficient numerical calculation of the absorption peak amplitudes and the dispersion-relation shapes.

DOI: 10.1103/PhysRevB.88.104431 PACS number(s): 75.78.−n, 75.70.Ak, 75.30.Cr, 76.50.+g

I. INTRODUCTION

Interlayer coupling is an important ingredient in several devices, such as spin valves[1,2] and magnetic tunnel junctions[3–6] (MTJs), multilayered materials, and any system based on two or more ferromagnetic layers separated by a nonmagnetic spacer. In spin valves and MTJs, strong interlayer coupling is a key issue for devices using synthetic free or pinned layers,[7–9] whereas, weak coupling is usually observed between the free and the pinned layers.[10–12] In both cases, the dynamic behavior is influenced by the strength of the interlayer coupling in both saturated and unsaturated magnetic states. This coupling has been studied extensively in the past by several experimental techniques as magnetization measurements and magnetoresistance,[13,14] ferromagnetic resonance (FMR),[15–18] Brillouin light scattering[19–21] (BLS), and others.[22,23]

An interesting and recent approach for studying the effect of interlayer coupling on the high-frequency response of materials and devices is the use of broadband ferromagnetic resonance. This technique is based on a vector network analyzer (VNA), and it is usually known as VNA-FMR.[24] With this technique [VNA-FMR (Ref. 24)], we are able to measure the dynamic properties (permeability or absorption) in a frequency range from a few MHz to dozens of GHz. Moreover, all measurements can be performed in a magnetic-field range $-H_{max} \leqslant 0 \leqslant +H_{max}$, where H_{max} can be adjusted from a few Oe to several kOe. Therefore, besides measuring the saturated states as in traditional FMR, a broadband measurement can be performed on unsaturated states and even at zero field.

Here, we study the static and dynamic properties of spin-valve systems using VNA-FMR and magnetometry measurements. Our samples consist of Py/Cu/Py/IrMn layers described as follows. The bottom Py = permalloy ($Ni_{81}Fe_{19}$) layer acts as a free magnetic layer (F), whereas, the top Py layer is coupled to an antiferromagnet ($Ir_{20}Mn_{80}$) and behaves as a pinned layer (P). We are able to analyze the behavior of each layer and the effect of the interaction mediated by the Cu spacer. By varying the Cu layer thickness t_{Cu}, we are able to control the interaction between the Py layers, producing new features on broadband spectra in unsaturated magnetic states. In particular, we observe complex dispersion relations, including frequency jumps and absorbed power intensities, depending on the oscillation modes.

A semianalytical model based on the magnetic free energy for the macrospin, together with the Landau-Lifshitz-Gilbert equation (LLG), is proposed and is applied to these systems. This model allows an efficient numerical calculation of the broadband absorption amplitudes and dispersion relations and describes the experimental results remarkably well. Moreover, the model provides further insight into magnetization dynamics of spin-valve-like systems in both saturated and unsaturated magnetic states.

II. EXPERIMENT

Spin valves with the structure Py (20 nm)/Cu(t_{Cu})/Py (20 nm)/IrMn (15 nm), where $t_{Cu} = 0.75$, 1.0, and 2.5 nm, were produced using magnetron sputtering on a Si(100) substrate with a Ta (5-nm) buffer and capping layers. The deposition conditions were 5-mTorr pressure and 50 sccm Ar gas flow after a 5×10^{-8}-Torr base pressure had been attained in the whole chamber. A rf power source was used for Py depositions, whereas, dc sources were used for Ta, Cu, and IrMn depositions. All deposition rates were calibrated by low angle x-ray reflectivity measurements. During the growth process, an in-plane magnetic field of about 200 Oe was applied in order to induce an unidirectional anisotropy at the ferromagnetic (FM)/antiferromagnetic (AFM) interface, leading to the pinning of the top FM layer through the exchange bias effect.

We performed static magnetic measurements (M vs H) with a vibrating sample magnetometer under dc fields of ±300 Oe. For the dynamic measurements, we used a broadband ferromagnetic resonance setup composed of a Rohde & Schwarz ZVA24 vector network analyzer, combined with a co-planar waveguide for frequencies in the range of 0.1–7.0 GHz and dc magnetic fields in the range of ±300 Oe. For these measurements, each sample was placed on top of a two port co-planar waveguide (CPW) where the external field H was applied along the propagation direction as shown in Fig. 1. The transmission S_{21} and reflection S_{11} coefficients were measured in the field and frequency ranges specified above. The absorbed

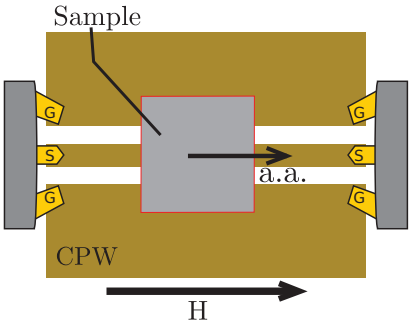

FIG. 1. (Color online) Schematic of the CPW structure and a sample placed on top of it. The central conductor of the CPW is about 260-μm wide. High-frequency microprobes and coaxial cables (not shown) were used to connect the structure to the VNA. The sample's anisotropy axis (a.a.) is aligned with the direction of the applied external field H.

power ratio in the waveguide was calculated as[25]

$$P_{\text{Loss}}/P_{\text{In}} = 1 - |S_{11}|^2 - |S_{21}|^2. \quad (1)$$

The ferromagnetic resonant spectra (magnetic absorption) were obtained by measuring this ratio with respect to a reference measurement of the dielectric losses, acquired with the sample saturated along the direction of the rf field.

III. EXPERIMENTAL RESULTS

Our samples were engineered so as to have distinct coupling intensities between their FM layers. From the static hysteresis loops, measured with the external field aligned with the easy magnetization axis (as shown in Fig. 2), we can clearly see how the thickness of the Cu spacer modulates the intensity of the coupling between the FM layers.

The sample with $t_{\text{Cu}} = 2.5$ nm [Fig. 2(a)] shows typical spin-valve behavior with well-known parallel and antiparallel magnetization states. Coming from negative saturation, the first layer to flip is the P layer at a field related to the unidirectional anisotropy, then the F layer flips at a field close to zero. This is observed in the magnetization curve as a shifted response for the P layer and a centered response for the F layer.

Such features indicate negligible coupling between the FM layers. On the other hand, for $t_{\text{Cu}} = 1.00$ nm [Fig. 2(b)], the coupling now manifests itself as a small shift (toward negative H) in the response of the F layer. A larger coupling is observed for $t_{\text{Cu}} = 0.75$ nm with a greater shift in the F-layer response, and the antiparallel state is no longer observed. Instead of that, a gradual rotation of the magnetization is now the main switching process.

The right side of Fig. 2 shows the measured absorbed power spectra for our samples. The color scale denotes the amplitude from blue (minimum) to red (maximum). The amplitude maxima on the branches correspond to the resonant modes. In these measurements, we can see two clear resonant responses [Fig. 2(b)] for the sample without coupling ($t_{\text{Cu}} = 2.50$ nm), one centered and the other field shifted, corresponding to the F and P layers, respectively. As already observed[26] in simple or exchange biased magnetic systems, the reversal of

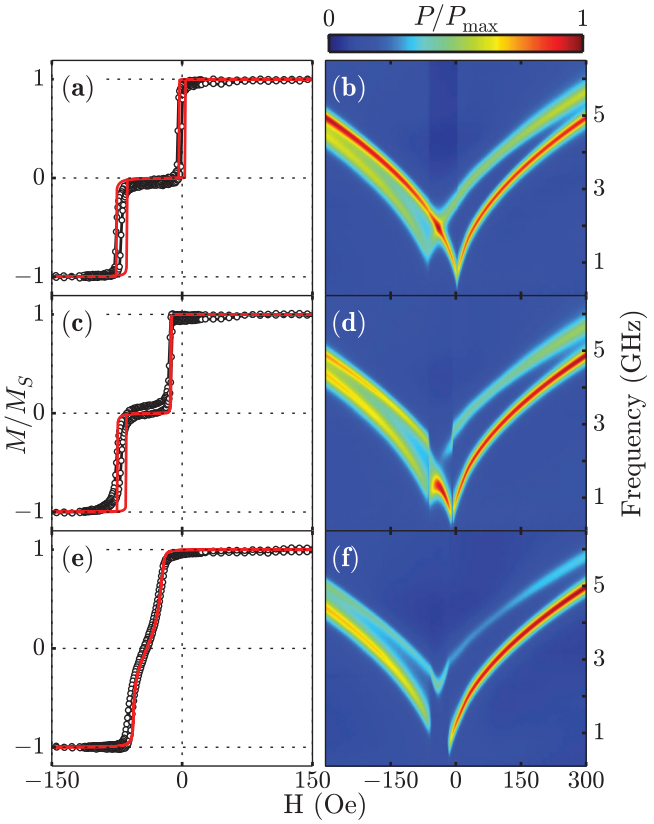

FIG. 2. (Color online) Measured and calculated magnetic hysteresis loops (left) and the broadband FMR spectra (right) for $t_{\text{Cu}} = 2.50$ nm (top), $t_{\text{Cu}} = 1.00$ nm (middle), and $t_{\text{Cu}} = 0.75$ nm (bottom). The symbols represent the experimental data, and the solid line is the calculated curve.

the slopes of the branches occurs at the switching fields of the respective layers. On the other hand, for the samples with coupled FM layers ($t_{\text{Cu}} = 1.00$ and $t_{\text{Cu}} = 0.75$ nm), a pair of resonant branches is still observed in parallel magnetization states, whereas, a completely different behavior is observed in unsaturated states, including frequency jumps in the resonant branches for both layers at their switching fields. These features will be addressed in Sec. V after we present our model and numerical calculations for these systems. In all cases (saturated and unsaturated samples), we observe different absorption intensities on each resonant branch. In order to gain further insight into the absorption of the saturated states, in Fig. 3, we plot the absorption profiles for these samples at 3.7 GHz. In this figure, four absorption peaks are observed for all samples. In the uncoupled case [Fig. 3(a)], the small peaks represent the oscillation of the P layer, whereas, the larger peaks are associated with the resonance of the F layer.

Therefore, the difference in height of the peaks can clearly be ascribed to the larger damping parameter α for the exchange biased P layer.[27] This is related to a broader linewidth, which results in a smaller peak height. For the samples in which FM layers interact [Figs. 3(b) and 3(c)], the inner peak amplitudes are reduced relative to the outer peaks without a significant increase in the measured linewidths (not shown), indicating that damping is not responsible for this behavior.

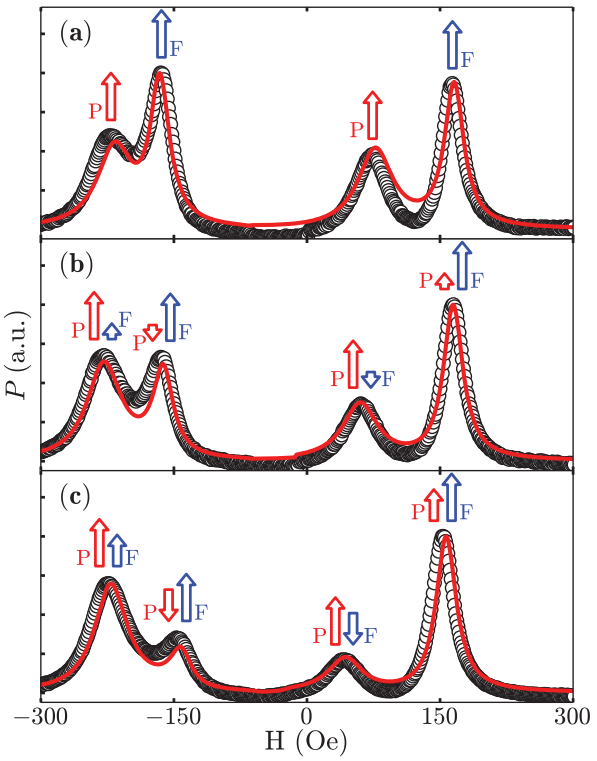

FIG. 3. (Color online) Absorbed power profiles at 3.7 GHz for samples with three different Cu spacer thicknesses: (a) $t_{Cu} = 2.5$, (b) $t_{Cu} = 1.0$, and (c) $t_{Cu} = 0.75$ nm. The symbols correspond to the experimental data, and the solid line corresponds to the calculated curve. The arrows represent the oscillating vectors (see Fig. 5 for further details).

This reduction depends on the coupling intensity, and it will be explained later in terms of our model and numerical calculations.

From Fig. 3 and thereafter, the filled arrows represent the magnetization vectors, whereas, empty arrows represent the oscillating vectors, and they were colored red and blue for the pinned and free layers, respectively.

IV. SEMIANALYTICAL MODEL AND NUMERICAL CALCULATIONS

In order to understand the features observed in our M vs H curves and broadband measurements, we have adopted a macrospin model that takes the usual free-energy density terms for each ferromagnetic layer plus a term describing the effective interaction between the free (F) and the pinned (P) layers into account as follows:

$$E = E_{\text{Pinned}} + E_{\text{Free}} + E_{\text{Interaction}}. \tag{2}$$

The perpendicular anisotropy term that appears in the free energy corresponds to the uniaxial anisotropy along the hard axis direction, which is perpendicular to the plane of the thin film.

The free-energy densities for the two layers E_{Pinned} and E_{Free} incorporate the Zeeman, in-plane uniaxial anisotropy, shape anisotropy, and out-of-plane anisotropy terms.

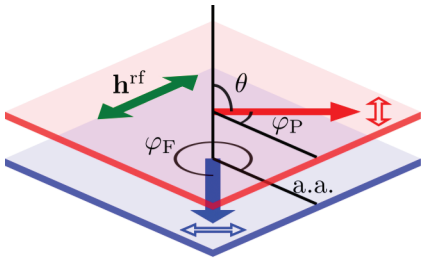

FIG. 4. (Color online) Sketch of the theoretical model adopted for the numerical calculations. The magnetization vectors (filled arrows) lie on the plane of the samples, their orientations being defined by angles θ and φ measured from the sample's normal and a.a., respectively. The oscillating vectors (empty arrows) are parallel to the $\hat{\varphi}$ directions (not shown). The radio-frequency field $\mathbf{h}^{\text{rf}}$ is also parallel to the sample and is perpendicular to the a.a.

Generally, out-of-plane anisotropy can be originated from surface roughness, crystalline ordering, or interface effects. E_{Pinned} also includes the exchange bias interaction term that keeps the corresponding layer pinned and the related rotatable anisotropy,[27] which arises from interfacial antiferromagnet grains with weak effective anisotropy and behaves like an anisotropy where the easy axis rotates toward the direction of the magnetization vector. In our system, as shown in Fig. 4, both layers have the same thickness t and saturation magnetization M_S, and we express the energy density in terms of the polar θ and azimuthal φ angles of the magnetizations and the anisotropy axis. Since the shape anisotropy energy is dominant in our system, the magnetization vector always lies on the plane of the thin film so that $\theta = \pi/2$. Also, considering that the anisotropies have an in-plane easy magnetization axis direction, parallel to $\varphi = 0$, and having applied the external field H applied at φ_H, then the normalized free-energy density ($\eta = E/M_S$) for the F and P layers, keeping only the φ dependent terms, can be written as follows:

$$\begin{aligned} \eta_{\text{Pinned}} &= -H\cos(\varphi_H - \varphi_P) - H_{\text{EB}}\cos(\varphi_P) - \tfrac{1}{2}H_k^P\cos^2(\varphi_P), \\ \eta_{\text{Free}} &= -H\cos(\varphi_H - \varphi_F) - \tfrac{1}{2}H_k^F\cos^2(\varphi_F), \end{aligned} \tag{3}$$

where H_k^P, H_k^F, φ_P, and φ_F are the uniaxial anisotropy fields and the in-plane magnetization angles of the P and F layers, respectively; H_{EB} is the exchange bias field acting on the pinned layer. The adopted interaction energy density reads

$$\eta_{\text{Int}} = -H_1^J\cos(\varphi_P - \varphi_F) + H_2^J\cos^2(\varphi_P - \varphi_F), \tag{4}$$

with $H_1^J = \frac{J_1}{tM_S}$ and $H_2^J = \frac{J_2}{tM_S}$, where J_1 and J_2 are the bilinear and biquadratic interaction constants between the two layers, respectively.

By minimizing $\eta = \eta_{\text{Pinned}} + \eta_{\text{Free}} + \eta_{\text{Int}}$ for a given H, the equilibrium angles φ_P and φ_F of the magnetization vectors can be deduced.

The magnetization dynamics in our system is described by the LLG equation adapted for our purpose,

$$\frac{d\mathbf{M}_i}{dt} = -\gamma(\mathbf{M}_i \times H_i) + \frac{\alpha_i}{M_S}\left(\mathbf{M}_i \times \frac{d\mathbf{M}_i}{dt}\right), \tag{5}$$

with $i = F, P$. Each layer is expected to follow this equation independently; hence, in angular coordinates, it can be expressed as

$$\begin{aligned} \frac{d\theta_i}{dt} &= \frac{\gamma}{(1+\alpha_i^2)}(H_{\varphi_i} + \alpha_i H_{\theta_i}), \\ \sin\theta_i \frac{d\varphi_i}{dt} &= \frac{\gamma}{(1+\alpha_i^2)}(\alpha_i H_{\varphi_i} - H_{\theta_i}), \end{aligned} \tag{6}$$

where H_φ and H_θ are the azimuthal and polar components of the effective field, α is the dimensionless damping parameter, and γ is the gyromagnetic ratio, which is the same for both layers. The effective field components can be expressed as

$$\begin{aligned} H_{\theta_i} &= -\frac{1}{M_S}\frac{\partial E}{\partial \theta_i} + \mathbf{h}^{\mathrm{rf}} \cdot \hat{\theta}_i, \\ H_{\varphi_i} &= -\frac{1}{M_S \sin\theta_i}\frac{\partial E}{\partial \varphi_i} + \mathbf{h}^{\mathrm{rf}} \cdot \hat{\varphi}_i, \end{aligned} \tag{7}$$

where $\mathbf{h}^{\mathrm{rf}}$ is the dynamic component of the applied external field, $\hat{\theta}_i = \cos\varphi_i \cos\theta_i \hat{x} + \sin\varphi_i \cos\theta_i \hat{y} - \sin\theta_i \hat{z}$, and $\hat{\varphi}_i = -\sin\varphi_i \hat{x} + \cos\varphi_i \hat{y}$.

In our specific case, $\sin\theta_P = \sin\theta_F = 1$, which means that we can rewrite Eq. (6) for the F and P layers as follows:

$$\begin{bmatrix} \dot{\theta}_P \\ \dot{\varphi}_P \\ \dot{\theta}_F \\ \dot{\varphi}_F \end{bmatrix} = -\frac{\gamma}{M_S}[\mathbf{\Lambda}] \begin{bmatrix} \partial E/\partial\theta_P \\ \partial E/\partial\varphi_P \\ \partial E/\partial\theta_F \\ \partial E/\partial\varphi_F \end{bmatrix} + \gamma[\mathbf{\Lambda}] \begin{bmatrix} \mathbf{h}^{\mathrm{rf}} \cdot \hat{\theta}_P \\ \mathbf{h}^{\mathrm{rf}} \cdot \hat{\varphi}_P \\ \mathbf{h}^{\mathrm{rf}} \cdot \hat{\theta}_F \\ \mathbf{h}^{\mathrm{rf}} \cdot \hat{\varphi}_F \end{bmatrix}, \tag{8}$$

where

$$[\mathbf{\Lambda}] = \begin{bmatrix} \frac{1}{1+\alpha_P^2}\begin{pmatrix} \alpha_P & 1 \\ -1 & \alpha_P \end{pmatrix} & 0 \\ 0 & \frac{1}{1+\alpha_F^2}\begin{pmatrix} \alpha_F & 1 \\ -1 & \alpha_F \end{pmatrix} \end{bmatrix}. \tag{9}$$

A. Susceptibility tensor

The differential susceptibility tensor $[\boldsymbol{\chi}] = d\mathbf{M}/d\mathbf{H}$ characterizes the dynamic magnetic response of a system to an external field. In our system, $[\boldsymbol{\chi}]$ gives us the relation between the radio-frequency field $\mathbf{h}^{\mathrm{rf}}$ and the oscillating part $\dot{\mathbf{M}}$ of the magnetization vectors,

$$\dot{\mathbf{M}}_F + \dot{\mathbf{M}}_P = [\boldsymbol{\chi}]\dot{\mathbf{h}}^{\mathrm{rf}}, \tag{10}$$

where $\dot{\mathbf{M}}_i = M_S[\dot{\theta}_i\hat{\theta}_i + \sin\theta_i\dot{\varphi}_i\hat{\varphi}_i]$ for each layer. In order to derive an equivalent expression as a function of the angular coordinates, we define $\mathbf{\Omega} = (\theta_P, \varphi_P, \theta_F, \varphi_F)$ with $\mathbf{\Omega} = \mathbf{\Omega}_0 + \delta\mathbf{\Omega}^{\mathrm{rf}}$, where $\delta\mathbf{\Omega}^{\mathrm{rf}} \propto e^{j\omega t}$ are small deviations around the equilibrium positions $\mathbf{\Omega}_0$. The magnetization deviations $\delta\mathbf{\Omega}^{\mathrm{rf}}$ are driven by the radio-frequency field $\mathbf{h}^{\mathrm{rf}}$; thus, they oscillate at the same frequency ω. The projections $\mathbf{h}^{\mathrm{rf}}_{\mathbf{\Omega}} = \mathbf{h}^{\mathrm{rf}} \cdot \hat{\Omega}_{\mathbf{0}}$ are related to the magnetization oscillations $\delta\mathbf{\Omega}^{\mathrm{rf}}$ by a pseudosusceptibility tensor $[\boldsymbol{X}]$, defined by

$$\delta\mathbf{\Omega}^{\mathrm{rf}} = [\boldsymbol{X}]\mathbf{h}^{\mathrm{rf}}_{\mathbf{\Omega}}. \tag{11}$$

Next, if we expand the energy terms around $\mathbf{\Omega}_0$ as in $\partial E/\partial\Omega_k^{\mathrm{rf}} = \sum_l \frac{\partial^2 E}{\partial\Omega_k \partial\Omega_l}\delta\Omega_l^{\mathrm{rf}}$, Eq. (8) can be expressed as

$$-\frac{\gamma}{M_S}[\mathbf{\Lambda}][\boldsymbol{E}_{\mathbf{\Omega}\mathbf{\Omega}}][\boldsymbol{X}]\mathbf{h}^{\mathrm{rf}}_{\mathbf{\Omega}} + \gamma[\mathbf{\Lambda}]\mathbf{h}^{\mathrm{rf}}_{\mathbf{\Omega}} = j\omega x[\boldsymbol{X}]\mathbf{h}^{\mathrm{rf}}_{\mathbf{\Omega}}, \tag{12}$$

where the matrix $[\boldsymbol{E}_{\mathbf{\Omega}\mathbf{\Omega}}]$ has elements $E_{\Omega\Omega kl} = \frac{\partial^2 E}{\partial\Omega_k\partial\Omega_l}$. For our particular system, the nonzero values of $[\boldsymbol{E}_{\mathbf{\Omega}\mathbf{\Omega}}]$ are as follows:

$$\begin{aligned} E_{\theta_P\theta_P} &= M_S\big[4\pi M_S - H_\perp + H\cos(\varphi_H - \varphi_P) + H_k^P \cos^2\varphi_P + H_{\mathrm{EB}}\cos\varphi_P + H_R + H_1^J\cos(\varphi_P - \varphi_F) - 2H_2^J\cos^2(\varphi_P - \varphi_F)\big], \\ E_{\varphi_P\varphi_P} &= M_S\big\{H\cos(\varphi_H - \varphi_P) + H_k^P\cos(2\varphi_P) + H_{\mathrm{EB}}\cos\varphi_P + H_R + H_1^J\cos(\varphi_P - \varphi_F) - 2H_2^J\cos[2(\varphi_P - \varphi_F)]\big\}, \\ E_{\theta_F\theta_F} &= M_S\big[4\pi M_S - H_\perp + H\cos(\varphi_H - \varphi_F) + H_k^F\cos^2\varphi_F + H_1^J\cos(\varphi_P - \varphi_F) - 2H_2^J\cos^2(\varphi_P - \varphi_F)\big], \\ E_{\varphi_F\varphi_F} &= M_S\big\{H\cos(\varphi_H - \varphi_F) + H_k^F\cos(2\varphi_F) + H_1^J\cos(\varphi_P - \varphi_F) - 2H_2^J\cos[2(\varphi_P - \varphi_F)]\big\}, \\ E_{\theta_P\theta_F} &= E_{\theta_F\theta_P} = -M_S\big[H_1^J + 2H_2^J\cos(\varphi_P - \varphi_F)\big], \\ E_{\varphi_P\varphi_F} &= E_{\varphi_F\varphi_P} = -M_S\big\{H_1^J\cos(\varphi_P - \varphi_F) + 2H_2^J\cos[2(\varphi_P - \varphi_F)]\big\}, \end{aligned} \tag{13}$$

where H_R and $H_\perp$ are the effective rotatable and perpendicular anisotropy fields. For an arbitrary field $\mathbf{h}^{\mathrm{rf}}$ oscillating at a frequency ω, we can obtain the pseudosusceptibility tensor from

$$[\boldsymbol{X}] = \left(j\frac{\omega}{\gamma}[\mathbf{\Lambda}]^{-1} + [\boldsymbol{E}_{\mathbf{\Omega}\mathbf{\Omega}}]\right)^{-1}. \tag{14}$$

This equation can be solved efficiently by standard numerical methods, resulting in the susceptibility tensor for each applied external field H and excitation frequency ω.

B. Resonant frequencies

Important features of our system are the resonant frequencies. These can be calculated from

$$\frac{\gamma}{M_S}[\mathbf{\Lambda}][\boldsymbol{E}_{\mathbf{\Omega}\mathbf{\Omega}}]\delta\mathbf{\Omega} = -j\omega_r\delta\mathbf{\Omega}. \tag{15}$$

This equation can be solved as an eigensystem by numerical methods. The eigenvalues provide us with the resonant frequencies ω_r and the eigenvector values of $\delta\mathbf{\Omega}$ at that frequency. Two positive values of ω_r are found for each external field H. The computed values of $\delta\mathbf{\Omega} = (\delta\theta_P, \delta\varphi_P, \delta\theta_F, \delta\varphi_F)$ show that the amplitude of the out-of-plane oscillations is negligible

($\delta\theta_P \approx \delta\theta_F \approx 0$) as expected. The analysis of the in-plane oscillations $\delta\varphi_P$ and $\delta\varphi_F$ of a given eigenvector allows us to determine which layer oscillates more strongly at the frequency of the corresponding eigenvalue. When $|\delta\varphi_P| > |\delta\varphi_F|$, we associate the resulting eigenvalue with natural resonant frequency ω_P of the pinned layer. In the opposite case of ($|\delta\varphi_P| < |\delta\varphi_F|$), it is associated with natural frequency ω_F of the free layer. It should be noted that $\delta\mathbf{\Omega}$ values, obtained by this method, are multiplied by an unknown amplitude and phase and, thus, are not suitable for calculating the absorbed power or to compare them at different fields H. However, they provide relevant information on the relative phase and amplitude of the oscillation of each layer over the dispersion relation.

C. Absorbed power

In order to compare our calculations directly with the experimental results, it is important to compute the average power absorbed by our system at a given field and frequency. We start by describing the instant power per unit volume absorbed by our system,

$$P = -\mathbf{h}^{\mathrm{rf}} \cdot (\dot{\mathbf{M}}_F + \dot{\mathbf{M}}_P). \tag{16}$$

It should be noted that the amplitude of P depends on three factors: (a) the relative orientation between $\mathbf{h}^{\mathrm{rf}}$ and the oscillating vectors $\dot{\mathbf{M}}_i$, (b) the temporal phase difference between $\dot{\mathbf{M}}_F$ and $\dot{\mathbf{M}}_P$, and (c) the relative orientation of the oscillating vectors, which depends on the direction of the magnetization at the equilibrium position for each layer. A graphical representation of several possible cases is presented in Fig. 5.

The average absorbed power per unit volume over an oscillatory cycle also depends on the temporal phase difference between $\mathbf{h}^{\mathrm{rf}}$ and the magnetization response and can be calculated by

$$\begin{aligned}\langle P\rangle &= -\omega M_S \mathrm{Im}\left[\sum_k h^{\mathrm{rf}}_{\Omega k}\delta\Omega^{\mathrm{rf}}_k\right] \\ &= -\omega M_S \mathrm{Im}\left[\sum_{k,l} h^{\mathrm{rf}}_{\Omega k} X_{kl} h^{\mathrm{rf}}_{\Omega l}\right].\end{aligned} \tag{17}$$

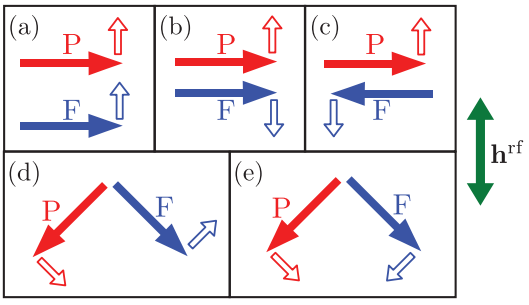

FIG. 5. (Color online) Geometrical representation of the magnetization vectors (filled arrows) and oscillating vectors (empty arrows). Magnetizations are shown in (a) and (b) parallel states, (c) antiparallel state, and (d) and (e) noncollinear states. The oscillations are in phase in (a), (c), and (d) and are out of phase in (b) and (e). For the shown $\mathbf{h}^{\mathrm{rf}}$, (a) and (e) should have greater absorbed power than (b), (c), or (d).

TABLE I. Parameters used in simulations.

Parameters common to all samples			
M_S (emu/cm^3)	800 (Ref. 28)		
γ (MHz/Oe)	17.59 (Ref. 28)		
α_{Pinned}	0.018		
α_{Free}	0.010		
H_K^F (Oe)	5		
H_K^P (Oe)	15		
H_R (Oe)	9		
Sample-dependent parameters			
t_{Cu}	2.5 nm	1.0 nm	0.75 nm
H_{EB} (Oe)	70	83	81
H_1^J (Oe)	0	13	35
H_2^J (Oe)	0	1.0	4.5
$H_\perp$ (Oe)	0	600	600
φ_H	4°	2°	5°

V. DISCUSSION

Here, we separate the discussion on samples that exhibit coupling between the ferromagnetic layers from that on the sample with uncoupled layers. The coupling strengths were obtained by comparing the calculated and experimental data. All simulation parameters are collected in Table I.

We chose the damping constants so that they reproduce the field widths observed at 3.7 GHz (see Fig. 3). No frequency dependence of the damping parameters was considered in this paper.

A. No coupling

When there is no coupling between the FM layers, our system behaves as two independent systems. The hysteresis loop can be treated as the sum of two square loops, one (centered) corresponding to F and the other (field shifted by H_{EB}) corresponding to P. The broadband response is also the sum of the individual responses of each layer. In our model, the matrix $[\boldsymbol{E}_{\mathbf{\Omega\Omega}}]$ is then formed by two independent matrix blocks along the main diagonal. Thus, an independent solution can be found for each block, corresponding to the F and P layers of our samples. The solutions for the resonant frequencies, when the damping is neglected, are the well-known Kittel relations,

$$\begin{aligned}\omega_r^P &= \gamma\sqrt{4\pi M_S - H_\perp \pm H \pm H_{\mathrm{EB}} + H_k^P + H_R} \\ &\quad\times\sqrt{\pm H \pm H_{\mathrm{EB}} + H_k^P + H_R}, \\ \omega_r^L &= \gamma\sqrt{4\pi M_S - H_\perp \pm H + H_k^F}\sqrt{\pm H + H_k^F},\end{aligned} \tag{18}$$

the $\pm$ sign being chosen according to the direction of the respective magnetic layer, $+$ for $\varphi = 0$ and $-$ for $\varphi = \pi$ corresponding to the right and left resonant branches experimentally observed. The resonant branches cross each other when the layers are in the antiparallel state and the external field is

$$H = H_0 = -\tfrac{1}{2}\left(H_{\mathrm{EB}} + H_k^P + H_R - H_k^F\right). \tag{19}$$

At this point, the total absorbed power is the sum of the power absorbed by each individual layer.

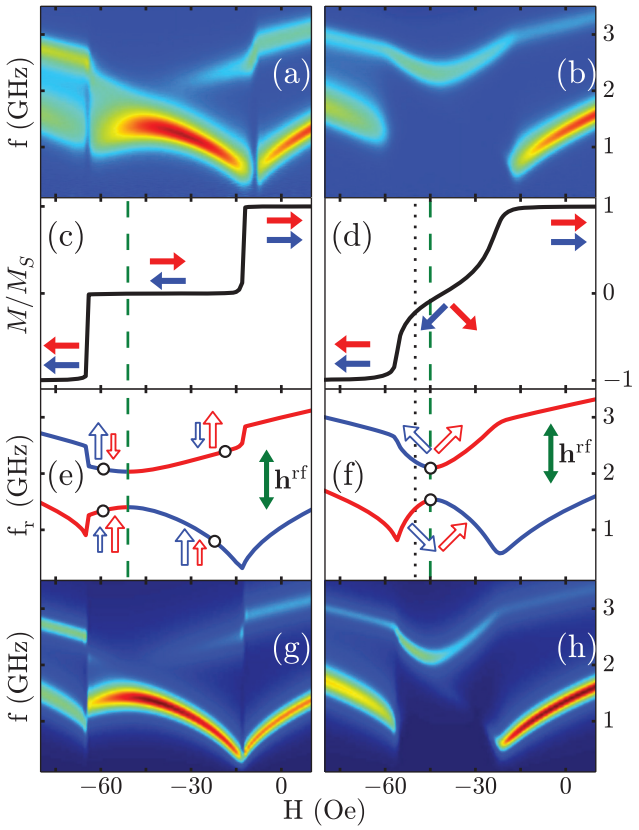

FIG. 6. (Color online) Experimental and simulation details in the unsaturated states for $t_{Cu} = 1.0$ nm (left) and $t_{Cu} = 0.75$ nm (right). (a) and (b) Experimental broadband spectra, (c) and (d) simulated magnetization curves (single branch), (e) and (f) simulated dispersion relation, and (g) and (h) simulated broadband average absorbed power. Filled arrows represent the magnetization vectors, and empty arrows represent the oscillating vectors at the marked circles.

B. Coupled FM layers

Figure 6 summarizes both the experimental and the numerical results on an expanded scale of H. In Figs. 6(a) and 6(b), we notice two arc-shaped (lower and upper) branches over the unsaturated regime. These features are reproduced by our model, resulting in the dispersion relations and the simulated broadband average absorbed power shown in panels (e)–(h).

Examining Figs. 6(c) and 6(d), we realize that the hysteresis response of the F layer is no longer centered. For a positive bilinear interaction ($J_1 > 0$), the loops of the F layer are field shifted toward the position of the P-layer loop. If the coupling is not large, as for the sample with $t_{Cu} = 1.0$ nm, the square shape of the loops is maintained, indicating that the magnetization flips between the parallel and the antiparallel directions with respect to the external field [Fig. 6(c)]. For the sample with $t_{Cu} = 0.75$ nm, whose coupling intensity is larger, the hysteresis loop is no longer square but, instead, acquires a rounded shape due to the simultaneous rotation of the FM layers [Fig. 6(d)]. These magnetization states along the magnetization curve were represented in the former figure as pairs of filled arrows.

When excited by an external rf field, the magnetization of each layer does not oscillate independently. Instead, they oscillate coherently with correlated amplitude and phase difference. In this case, we find that, for a resonant mode with frequency f_r, the phase difference of the oscillations $\Delta\phi = \arg[\delta\varphi_F] - \arg[\delta\varphi_P]$ depends on the natural frequency of the companion layer: A natural frequency higher or lower than f_r gives rise to a phase difference of $\Delta\phi \approx 0^\circ$ or $\Delta\phi \approx 180^\circ$, respectively. This information is depicted in Figs. 6(e) and 6(f) where the resonant modes, classified (see Sec. IV B) in terms of the dominant contribution for the oscillation, are represented by the red and blue lines associated with the P and F layers, respectively. The pairs of empty arrows represent the oscillating vectors at the indicated open black circles, drawn using the scheme of Fig. 5.

Irrespective of the coupling intensity, there is an external field value H_0 where both layers oscillate at the same frequency (see the green dashed line in Fig. 6). As long as the antiparallel state holds, which is the case for $t_{Cu} = 1.0$ nm, this field takes the same value as in the uncoupled case [see Eq. (19)]. In all other cases as for $t_{Cu} = 0.75$ nm, the magnetization angles must be taken into account to calculate H_0, giving a complicated analytical expression. The resulting values are, however, usually close to the former cases (see the dotted line on the right panel of Fig. 6). At this field H_0, two resonant frequencies, rather than one as in the uncoupled case, are found. The gap between these frequencies is proportional to the intensity of the given coupling. In this magnetization state, both layers oscillate with the same amplitude ($|\delta\varphi_P| = |\delta\varphi_F|$) at any given frequency. This may indicate that the dominant interaction in this state is the coupling energy.

For $t_{Cu} = 1.0$ nm, the lower arc in the dispersion relation is formed by oscillating modes where $\Delta\phi \approx 180^\circ$, but due to the antiparallel magnetization state, the resulting oscillating vectors are in the same direction and are parallel to $\mathbf{h}^{rf}$, favoring the absorption in this arc. On the other hand, in the upper arc, $\Delta\phi \approx 0^\circ$, and the oscillating vectors are in opposite directions. The relative amplitudes of the oscillating vectors vary gradually on the upper arc resonant modes. Therefore, our simulations describe the observed experimental spectra well. When the amplitude difference of the oscillating vectors is appreciable, e.g., at the marked circles in Fig. 6(e), a weak but clear absorption response is observed. This response gradually vanishes as the applied field approaches H_0 where both layers oscillate with the same amplitude. The similar oscillating amplitude transition occurs on the lower arc; in this case, it can be observed as a gradual change in the linewidth of the arc, starting from a broad linewidth at the left where the P-layer oscillation dominates toward a sharper linewidth at the right side of the spectrum where the F-layer oscillation dominates.

The sample with $t_{Cu} = 0.75$ nm shows an appreciable absorption only in the upper inverted arc. Here, the oscillating vectors [shown in Fig. 6(f) as calculated at H_0] are no longer parallel to the rf field. Instead, their vector sum is nearly parallel to the rf field for the upper branch and is nearly perpendicular to the rf field for the lower arc.

We are now able to understand the behavior of the peak amplitudes shown in Figs. 3(b) and 3(c). When the calculated oscillating vectors shown on top of each peak are in opposite directions, the peak amplitude decreases. The smaller the oscillating amplitude difference, the larger the decrease in amplitude.

VI. CONCLUSIONS

To summarize, we have reported the broadband resonance spectra in coupled and uncoupled magnetic layers in a single spin-valve configuration, namely, NiFe (20 nm)/Cu(t_{Cu})/NiFe (20 nm)/IrMn (15 nm), where $t_{Cu} = 0.75$, 1.0, or 2.5 nm controls the coupling intensity. In coupled cases, we observed that, at low field, the experimental broadband spectra were complex, whereas, at high field, the spectra showed the typical behavior of coupled saturated samples. The coupling between the ferromagnetic layers was observed to modify the relative amplitudes of the absorption peaks.

We were able to reproduce the broadband experimental results remarkably well, both in saturated and in unsaturated states, by employing a numerical method based on the macrospin approximation. Using our method, we obtained the dispersion relations [Eq. (15)] and the broadband average absorbed power [Eq. (17)]. The method provides further insight into the magnetization dynamics in coupled systems, predicting frequency gaps and complex dispersion relations in unsaturated magnetic states. Such states, despite their importance in applications, are usually neglected by the traditional descriptions of both regular FMR and broadband FMR experiments.

As a final comment, we would like to point out that our matrix mathematical approach easily enables the description of magnetic systems with an arbitrary number of interacting macrospins. It also permits an easy and fast software implementation of the method by using well-established numerical subroutines.[29]

ACKNOWLEDGMENTS

The authors thank Dr. M. Assolin Corrêa for the fruitful discussion and revision. This work was supported by the Brazilian agencies CNPq, FINEP, FAPERJ, and CAPES.

[1] B. Dieny, V. S. Speriosu, S. S. P. Parkin, B. A. Gurney, D. R. Wilhoit, and D. Mauri, Phys. Rev. B **43**, 1297 (1991).
[2] T. Shinjo and H. Yamamoto, J. Phys. Soc. Jpn. **59**, 3061 (1990).
[3] J. S. Moodera, L. R. Kinder, T. M. Wong, and R. Meservey, Phys. Rev. Lett. **74**, 3273 (1995).
[4] T. Miyazaki and N. Tezuka, J. Magn. Magn. Mater. **139**, L231 (1995).
[5] S. S. P. Parkin, C. Kaiser, A. Panchula, P. M. Rice, B. Hughes, M. Samant, and S.-H. Yang, Nature Mater. **3**, 862 (2004).
[6] S. Yuasa, T. Nagahama, A. Fukushima, Y. Suzuki, and K. Ando, Nature Mater. **3**, 868 (2004).
[7] H. van den Berg, W. Clemens, G. Gieres, G. Rupp, W. Schelter, and M. Vieth, IEEE Trans. Magn. **32**, 4624 (1996).
[8] J. L. Leal and M. H. Kryder, J. Appl. Phys. **83**, 3720 (1998).
[9] A. Veloso and P. P. Freitas, J. Appl. Phys. **87**, 5744 (2000).
[10] T. G. S. M. Rijks, R. Coehoorn, J. T. F. Daemen, and W. J. M. de Jonge, J. Appl. Phys. **76**, 1092 (1994).
[11] J. Faure-Vincent, C. Tiusan, C. Bellouard, E. Popova, M. Hehn, F. Montaigne, and A. Schuhl, Phys. Rev. Lett. **89**, 107206 (2002).
[12] T. Katayama, S. Yuasa, J. Velev, M. Ye. Zhuravlev, S. S. Jaswal, and E. Y. Tsymbal, Appl. Phys. Lett. **89**, 112503 (2006).
[13] S. S. P. Parkin, N. More, and K. P. Roche, Phys. Rev. Lett. **64**, 2304 (1990).
[14] S. S. P. Parkin, Phys. Rev. Lett. **67**, 3598 (1991).
[15] J. J. Krebs, P. Lubitz, A. Chaiken, and G. A. Prinz, Phys. Rev. Lett. **63**, 1645 (1989).
[16] B. Heinrich, J. F. Cochran, M. Kowalewski, J. Kirschner, Z. Celinski, A. S. Arrott, and K. Myrtle, Phys. Rev. B **44**, 9348 (1991).
[17] B. Heinrich, Z. Celinski, J. F. Cochran, A. S. Arrott, K. Myrtle, and S. T. Purcell, Phys. Rev. B **47**, 5077 (1993).
[18] R. L. Rodríguez-Suárez, S. M. Rezende, and A. Azevedo, Phys. Rev. B **71**, 224406 (2005).
[19] G. Gubbiotti, G. Carlotti, A. Montecchiari, M. De Crescenzi, R. Zivieri, L. Giovannini, and F. Nizzoli, Phys. Rev. B **62**, 16109 (2000).
[20] R. J. Hicken, A. J. R. Ives, D. E. P. Eley, C. Daboo, J. A. C. Bland, J. R. Childress, and A. Schuhl, Phys. Rev. B **50**, 6143 (1994).
[21] S. M. Rezende, C. Chesman, M. A. Lucena, A. Azevedo, F. M. de Aguiar, and S. S. P. Parkin, J. Appl. Phys. **84**, 958 (1998).
[22] M. Belmeguenai, T. Martin, G. Woltersdorf, M. Maier, and G. Bayreuther, Phys. Rev. B **76**, 104414 (2007).
[23] A. M. Kaiser, C. Schöppner, F. M. Römer, C. Hassel, C. Wiemann, S. Cramm, F. Nickel, P. Grychtol, C. Tieg, J. Lindner, and C. M. Schneider, Phys. Rev. B **84**, 134406 (2011).
[24] W. Barry, IEEE Trans. Microwave Theory Tech. **34**, 80 (1986).
[25] H. Garcia-Miquel, M. Esbri, J. Andrés, J. Garcia, J. Garcia-Beneytez, and M. Vázquez, IEEE Trans. Magn. **37**, 561 (2001).
[26] C. Bilzer, T. Devolder, J.-V. Kim, C. Chappert, M. Ruehrig, and L. Baer, J. Appl. Phys. **106**, 063918 (2009).
[27] R. D. McMichael, M. D. Stiles, P. J. Chen, and W. F. Egelhoff, Phys. Rev. B **58**, 8605 (1998).
[28] M. Najafi, B. Krüger, S. Bohlens, M. Franchin, H. Fangohr, A. Vanhaverbeke, R. Allenspach, M. Bolte, U. Merkt, D. Pfannkuche, D. P. F. Möller, and G. Meier, J. Appl. Phys. **105**, 113914 (2009).
[29] E. Jones, T. Oliphant, P. Peterson *et al.*, "SciPy: Open Source Scientific Tools for Python" (2001), see http://www.scipy.org/.